J. Fluid Mech. (2013), *vol.* 724, *pp.* 5–35. © Cambridge University Press 2013
doi:10.1017/jfm.2013.87

Rain-induced attenuation of deep-water waves

William L. Peirson[1],†, José F. Beyá[1,2], Michael L. Banner[3], Joaquín Sebastián Peral[4] and Seyed Ali Azarmsa[5]

[1]Water Research Laboratory, School of Civil and Environmental Engineering, The University of New South Wales, Manly Vale, NSW 2093, Australia

[2]Escuela de Ingeniería Civil Oceánica, Facultad de Ingeniería, Universidad de Valparaíso, Av. Brasil 1786 of. 30, Valparaíso, Chile

[3]School of Mathematics and Statistics, The University of New South Wales, Sydney 2052, Australia

[4]AREVA Wind GmbH Am Lunedeich 156 D-27572 Bremerhaven, Germany

[5]Faculty of Marine Sciences, Tarbiat Modares University, PO Box: 14115-111, Tehran, Iran

(Received 17 December 2010; revised 23 January 2013; accepted 9 February 2013; first published online 29 April 2013)

A laboratory investigation has been undertaken to quantify water wave attenuation rates as a function of rainfall rate. Vertical artificial rainfall is shown to generate weak near-surface velocity fluctuations that decline systematically away from the free surface and are independent of rainfall rate across the range of rainfall rates investigated (40–170 mm h^{-1}). In the absence of rain, the observed attenuation of gravity waves is at levels consistent with classical viscous theory, but with a systematic finite-amplitude effect observed above a mean steepness of 0.10. Wave attenuation rates were found to be independent of the mean wave steepness and identical when artificial rainfall rates of 108 and 141 mm h^{-1} were applied. Reassessment of complementary theoretical and experimental studies of individual droplets impacting on undisturbed water surfaces indicates that above a weak threshold rainfall rate of 30 mm h^{-1}, the surface irradiation becomes so frequent that droplet-generated violent surface motions directly interact with the incoming droplets. Present evidence is that a matching of time scales develops between the incoming surface irradiation and surface water motions generated by antecedent droplets as the rainfall rate increases. Consequently, at high rainfall rates, a highly dissipative surface regime is created that transmits little of the incident rainfall kinetic energy to the aqueous layers below. Rainfall-induced wave attenuation rates are compared with measurements of other wave attenuation processes to obtain a hierarchy of strength in both the laboratory and the field. Comparison is also made with wave attenuation theories that incorporate momentum and energy flux considerations. Rain-induced wave attenuation rates are weak or very strong depending on whether they are expressed in terms of energy scaling obtained from above or below the surface respectively, due to the high dissipation rate that occurs in the vicinity of the interface.

Key words: air/sea interactions, wave-turbulence interactions, waves/free-surface flows

---

† Email address for correspondence: w.peirson@unsw.edu.au

1. Introduction

This contribution addresses an enigma of air–water interfacial behaviour: theoretical studies of rain–wave interactions predict that water wave attenuation rates should depend linearly on the rain rate whereas laboratory studies to date show that wave attenuation rates are independent of the rain rate.

The role of rain in calming the sea is well known amongst mariners and was first studied by Reynolds (1874). Reynolds proposed that rain attenuates waves by generating subsurface vortex rings that disrupt wave motions in the surface layer.

Le Méhauté & Khangaonkar (1990) developed a theoretical approach that included the effect of rain on waves based on the momentum exchange from the wind and raindrops impacting the surface at different angles. For vertical rain falling on deep-water waves, their model predicted a non-dimensional rate of wave attenuation that depended linearly on rain intensity:

$$\frac{1}{\omega E(\omega)}\frac{\mathrm{d}E(\omega)}{\mathrm{d}t} = -\frac{3\rho_{rain}Ik}{\rho\omega}, \tag{1.1}$$

where ω is the angular wave frequency of waves of wavenumber k, E is the local wave energy density, t is time, I is rain intensity (the volumetric flux rate of water impacting per unit area of surface), ρ_{rain} and ρ are the densities of the rain and the fluid surface respectively (assumed to be equal during the present study).

In contrast with Le Méhauté & Khangaonkar (1990), Tsimplis (1992) found by experiment that attenuation rates were independent of rainfall intensity. His investigations of water wave attenuation due to rain were undertaken in a 2.35 m long, 0.15 m wide tank with 0.1 m water depth using monochromatic, mechanically-generated waves with frequencies between 15.7 and 31.5 rad s^{-1}. Attenuation rates were obtained from wave gauges located immediately adjacent to a fetch length of 0.55 m irradiated with rainfall rates of 300 and 600 mm h^{-1} from an array of hypodermic needles, yielding mean drop sizes of 3.61 mm and falling a distance of 1.75 m before impacting the surface. Tsimplis found that attenuation rates systematically increased with wave frequency ω, independent of wave steepness, with an equivalent constant eddy viscosity ν_E of $0.3\pm0.15\times10^{-4}$ m^2 s^{-1} defined to conform to the Lamb (1932) deep-water expression:

$$\frac{1}{\omega E(\omega)}\frac{\mathrm{d}E(\omega)}{\mathrm{d}t} = -\frac{c_g\Delta_R(\omega)}{\omega} = -\frac{4\nu_E k^2}{\omega}, \tag{1.2}$$

where c_g is the (assumed) linear group velocity of the waves, Δ_R is a spatial rain-induced attenuation coefficient and ν_E is a viscosity. In Lamb's original expression, ν_E is the molecular viscosity (denoted as ν hereafter). Tsimplis used ν_E to denote an eddy viscosity that parameterizes (presumed) turbulent processes in the water.

The rain-induced attenuation coefficient is obtained conventionally from measurements of wave energy via:

$$\Delta_R(\omega) = \Delta_T(\omega) - \Delta_\nu(\omega), \tag{1.3}$$

where Δ_ν is the wave attenuation coefficient characteristic of viscous effects and Δ_T is the total spatial wave attenuation coefficient defined by:

$$E(\omega) = E_0(\omega)\exp[-\Delta_T(\omega)x], \tag{1.4}$$

where x is fetch along the tank and E_0 is an initial reference-level wave energy.

Poon, Tang & Wu (1992) measured the attenuation coefficient of wind-generated waves under rain in an oval recirculating wind-wave tank of water depth 0.24 m, 0.31 m width, 0.445 m height and 19.7 m perimeter. The attenuation rates were obtained from changes in spectral energy measured using capacitance probes across a 1 m fetch irradiated with 2.6 mm mean diameter raindrops falling from an array of hypodermic needles 0.2 m above the mean water surface at rates of 35, 65 and 100 mm h^{-1}. The surface water waves were generated by winds of 3.4, 4.9 and 6.3 m s^{-1}. Poon *et al.* (1992) obtained higher attenuation coefficients than Tsimplis (1992) in spite of much lower incident rainfall rates. Although Poon *et al.* (1992) concluded that attenuation rate depended on rainfall intensity, they drew this conclusion by comparing their results with the Tsimplis & Thorpe (1989) values, which subsequently were revised downwards by Tsimplis (1992). Figure 10 in Poon *et al.* (1992) shows no systematic or significant change in wave attenuation rates with rainfall rate, thereby corroborating the Tsimplis finding of independence of wave attenuation rates with regard to rain intensity.

This fundamental incompatibility between the studies of Le Méhauté & Khangaonkar (1990) and Tsimplis (1992) is perplexing and Tsimplis recommended that studies of rainfall-induced, near-surface turbulence be undertaken to resolve its fundamental cause. To our knowledge, no previous investigation has specifically followed Tsimplis's recommendation to resolve this incompatibility. However, there have been recent and relevant investigations of rain-generated waves and near-surface fluctuating motions.

Bliven, Sobieski & Craeye (1997) measured the radar and wave response of water surfaces irradiated by rain and found a weak dependence of both radar return and high-frequency wave motions. The response of both radar return and high-frequency wave motions to changes in rain rate became significantly weaker at higher rainfall rates. Craeye & Schlüssel (1998) developed a theoretical description of surface renewal due to rainfall. Ho *et al.* (2000) and Zappa *et al.* (2009) reported turbulent dissipation measurements near water surfaces irradiated vertically by raindrops of natural sizes falling at close to terminal velocity to determine relationships between near-surface turbulent dissipation and gas exchange.

Braun (2003) measured near-surface fluctuating velocity intensities under rain-irradiated water surfaces in two separate experimental facilities. Acoustic Doppler velocimeter (ADV) measurements were carried out in a tunnel 26 m long, 1 m wide and 1.5 m in total depth exposed to 40 mm h^{-1} of needle-generated 2.9 mm diameter rainfall from a height of 4.5 m over a total fetch length of 2.3 m. The root-mean-square (r.m.s.) fluctuating velocities were of order 0.02 m s^{-1} decreasing systematically with depth. Particle image velocimetry (PIV) measurements yielded fluctuating velocities in a still water tank with 2.9 and 2.1 mm diameter drops falling at respective rain rates of 8 and 216 mm h^{-1}.

Rain effects are of considerable interest in their own right, particularly for understanding the remotely sensed behaviour of rain-forced seas. However, associated wider issues of wave–turbulence interactions have implications for the air–sea interaction and the general behaviour of multiphase air–water interfaces.

Detailed experimental investigations of possible coupling between waves and highly rotational near-surface motions expanded greatly during the 1970s and 1980s and followed two primary approaches. Some investigators focused on observations of wind- and wave-coupled rotational processes with consequent significant enhancement of exchange of momentum and constituents within the aqueous surface layers (e.g. Jones & Toba 2001; Komori, Nagaosa & Murakami 1993). Others explored the mechanical coupling between waves and the near-surface turbulent field via the interacting

Reynolds stresses (Cheung & Street 1988, hereafter CS 1988; Magnaudet & Thais 1995, hereafter MT 1995).

Boyev (1971) proposed a model for the attenuation of low-amplitude deep-water surface waves by intense subsurface turbulence, but was unable to find suitable data to verify his model. Belcher, Harris & Street (1994) and Harris, Belcher & Street (1996) reported theoretical and numerical analyses. They found that wave–turbulence interactions reduced net wind-induced wave growth to approximately 50 % of the wind energy input. At greater depths, where the turbulence becomes rapidly distorted, Teixeira & Belcher (2002, hereafter TB 2002) predicted theoretically that wave attenuation by turbulence would remove energy from the wave field at a rate approximately 33 % of the rate at which energy is fed to the wave field by the wind. TB 2002 calibrated their expressions against the measurements of wave attenuation rates in the presence of subsurface grid-generated turbulence by Ölmez & Milgram (1992).

Parallel work on swell dissipation by subsurface turbulence (Jenkins 1987; Ardhuin & Jenkins 2006, hereafter AJ 2006) has been directed at determining background levels of attenuation rate within spectral wave models (e.g. Tolman 2009, p. 32). Critically reviewing TB 2002, AJ 2006 agreed with the TB 2002 form but with a different theoretical foundation. AJ 2006 (pp. 553 and 554) obtained an attenuation rate that is approximately 20 % of the TB 2002 level. Ardhuin *et al.* (2010) provide a recent summary of the outcomes of these dissipation investigations.

Wave–aqueous turbulence interactions have assumed greater significance in recent numerical characterizations of breaking that appeal to eddy viscosity concepts (Tian, Perlin & Choi 2010). Such approaches contrast sharply with conventional understanding of spilling breaking (Duncan 1981, 1983; Banner 1988) and plunging breaking (Drazen, Melville & Lenain 2008) which show plausible energy losses computed from hydrodynamic descriptions of wave crest behaviour and without detailed consideration of wave–turbulence interactions.

In the laboratory, Peirson, Garcia & Pells (2003) measured much higher wave attenuation rates by opposing wind than would be anticipated from drag considerations, suggesting that wave–turbulence interactions are stronger than the rates estimated by TB 2002.

Although considerable progress has been made in understanding wave–turbulence interactions over the past 40 years, considerable gaps remain. Robust quantitative descriptions that characterize interactions between turbulence and waves and, specifically, between waves and rain are unavailable. There are two principal obstacles to directly resolving the magnitude of these interactions. First, the zone of highest wave velocities and turbulent activity lies above the wave troughs, a region where it has proved difficult to obtain reliable direct measurements of the Reynolds stresses (CS 1988; Rapp & Melville 1990, MT 1995; Siddiqui & Loewen 2007; Gemmrich 2010). The second major experimental challenge has been developing suitable control test conditions in which turbulent intensity decreases away from the surface (CS 1988) rather than decreasing away from a subsurface generation source (e.g. Ölmez & Milgram 1992).

In this contribution, artificial rain was used to generate a surface field of fluctuating velocities which were shown to decrease in intensity away from the free surface. The rain was directed vertically downward yielding no net input of horizontal momentum to the wave field. Monochromatic waves of different frequencies were propagated through the rain-perturbed zone to determine the attenuation rates quantitatively.

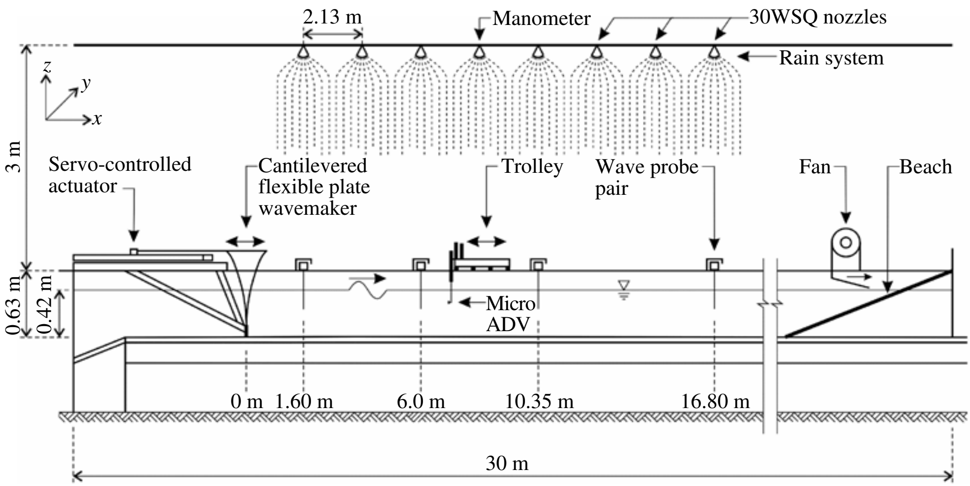

FIGURE 1. Schematic diagram showing experimental layout and key equipment (not to scale).

By increasing the monochromatic wave amplitude, finite-amplitude effects were also quantified.

Table 1 presents a brief overall summary of the principal reported investigations in relation to rain interactions with surface water waves.

In the next section, the experimental techniques are described, followed by a discussion of the present results in the context of other studies while exploring their implications for air–sea interaction. In the final section, the primary conclusions and recommendations are summarized.

2. Experimental equipment and methods

Facility

The test facility was the wave tank (30 m long, 0.6 m wide and 0.63 m total depth) with glass sidewalls (figure 1) that was used for the recent study of Banner & Peirson (2007). A programmable servo-controlled actuator drives a flexible plate wave generator cantilevered at the tank floor. For this study, only monochromatic waves were generated. Waves were absorbed at the end of the tank by a gently sloping beach. The mean water depth was maintained at 415 ± 1 mm for all experiments by an automatic control system. Over the measurement period, the water temperature varied from 10.9 to 12 °C.

Rainfall intensity can be characterized by two primary quantities. The rainfall rate is given by:

$$I = \frac{\pi}{6}\int_0^\infty \phi^3 n(\phi) w_R(\phi)\,\mathrm{d}\phi, \tag{2.1}$$

where ϕ is the rain drop diameter, $n(\phi)$ is the drop size distribution and $w_R(\phi)$ is the mean drop impact velocity (Craeye & Schlüssel 1998, equation (8)). An alternative and better characterization may be rainfall energy flux $\dot{E}_{rain}$:

$$\dot{E}_{rain} = \frac{\pi\rho_{rain}}{12}\int_{\phi_c}^\infty \phi^3 n(\phi) w_R^3(\phi)\,\mathrm{d}\phi, \tag{2.2}$$

Investigators	Facility	Rainfall rates (mm h^{-1})	Comments relevant to this study
Reynolds (1874)		Theoretical	Identified rain-generated turbulence as a mechanism for wave attenuation
Manton (1973)		Theoretical	Eddy viscosity model for wave attenuation due to rain
Houk & Green (1976)	Still tank hypodermic needle rain simulator (0.64 × 0.64 m area, 14 m fall height, 0.5 m water depth)	4–35	Surface waves generated by rain
Green & Houk (1979)	Still tank hypodermic needle rain simulator (0.62 width, 14 m fall height, water depth 0.5 m)	3–37	Mixing layer and surface waves caused by rain
Nystuen (1990)		Theoretical	Eddy viscosity model for wave decay due to rain
Le Méhauté & Khangaonkar (1990)		Theoretical	Momentum exchange model for wave decay due to wind and rain
Poon *et al.* (1992)	Circular wind–wave tank, hypodermic needle rain simulator (1 m fetch, fall 0.2 m height, 0.24 m water depth)	35–100	Wind wave attenuation due to wind and rain
Tsimplis (1992)	Wave tank hypodermic needle rain simulator (0.55 m fetch, 1.75 m fall height, 0.1 m water depth)	300, 600	Wave attenuation due to rain

TABLE 1. (Continued on next page)

Investigators	Facility	Rainfall rates (mm h^{-1})	Comments relevant to this study
Bliven *et al.* (1997)	Still tank hypodermic needle rain simulator (4 × 4 m area, 17 m fall height, 0.8 m water depth)	5–200	Surface waves generated by rainfall, radar scatter
Craeye & Schlüssel (1998)		Theoretical	Wave attenuation model based on kinetic energy flux and friction velocity
Ho *et al.* (2000)	Still tank hypodermic needle rain simulator (4 × 4 m area, 17 m fall height, 0.53 m water depth)	14–115	Gas exchange and its relation to turbulence generated by rain
Braun (2003)	Still tank hypodermic needle rain simulator (2.3 × 1 m area, 4.5 m fall height, water depth <1.5 m, ADV)^{1} and (3.9 m fall height PIV)^{2}	$(40)^{1}$ $(8, 216)^{2}$	Near-surface fluctuating velocity profile measurements, radar scatter, wind and rain.
Zappa *et al.* (2009)	Still tank nozzle rain simulator (45 × 19 m area, 10 m fall height, water depth <6 m)	25–50	Gas exchange and its relation to near-surface turbulence dissipation
Present study	Wave tank nozzle rain simulator (17 m fetch, 3 m fall height at terminal velocity, 0.4 m water depth)	108,141	Fluctuating velocity profile measurements, wave attenuation measurements

TABLE 1. Summary of investigations of rain–wave interactions.

where ϕ_c is the critical diameter for surface puncture. Droplet puncture of the surface occurs above a critical Weber number of 10, where the Weber number W is given by:

$$W = \frac{\rho_{rain}\phi w_R^2(\phi)}{\sigma} \tag{2.3}$$

and σ is the surface tension of the interface being punctured (Liow 2001).

For uniform drop size distributions, (2.2) becomes (Tsimplis 1992):

$$\dot{E}_{rain} = 0.5\rho_{rain} I w_R^2. \tag{2.4}$$

Previous studies have employed needle-based droplet generators, which have four primary characteristic limitations, namely:

(i) To achieve the velocities that are close to terminal and yield droplets that might be anticipated to reproduce essential surface penetrating behaviours, they must be installed at substantial ($O(20\ \text{m})$) heights above the irradiated surface. This exposes personnel to particular working hazards.

(ii) They preferentially irradiate the same location on the water surface, a characteristic not shared by real rainfall.

(iii) For systematic investigations, they are constrained to a single droplet size during any given test.

(iv) Their application has been restricted to relatively small irradiated areas due to the significant expense in their construction and the complexities of installing heavy water reservoirs at height.

In this investigation, an alternative approach was adopted which eliminated some of the limitations of needle-based generators and enabled measurement of wave attenuation rates (1.3) over a fetch length a factor of 8 larger than adopted by previous studies.

Vertical artificial rain was generated by duplicating the simulator developed by Shelton, von Bernuth & Rajbhandari (1985) who found that it was possible to produce droplet fields that were near-uniform spatially, with size distributions similar to natural rainfall and falling at terminal vertical velocities across a range of rain intensities from 85 to 168 mm h^{-1}. To duplicate the Shelton *et al.* system, eight 30WSQ nozzles were installed at 3.00 m above the tank surface located with a spacing of 2.13 m along the tank. Separate water and air manifold systems supplied pressurized air and water immediately upstream of the nozzles, the compressed air increasing the exit velocity of the water droplets. Water from the wave tank was recirculated through the rainfall system. The mean rainfall rate was controlled by a rotameter. For each rainfall case, the test conditions were established for 20 min prior to any measurements being taken. Rainfall intensity and uniformity was monitored during the experiments by visual inspection and temporary rain gauges located along the tank.

During this investigation, wave measurements were undertaken for two rainfall conditions: 108 ± 7 and 141 ± 6 mm h^{-1}. These conditions were achieved by setting the flow rates and nozzle pressures in accordance with the values in tables 4 and 5 of Shelton *et al.* (1985) that matched the droplet size distributions shown in their figures 4 and 5. At these rainfall rates, the high levels of spatial uniformity tabulated by Shelton *et al.* were verified. At rainfall rates outside this range, rainfall was less uniform along the entire tank and the system was only used to characterize the aqueous turbulence structure at a point directly beneath the central nozzle. For rainfall rates outside the 108–141 mm h^{-1} range, the stated rainfall rate is that recorded directly beneath the nozzle.

During the investigation, the droplet size distributions in figures 4 and 5 of Shelton *et al.* (1985) were assumed as well as their claim that the droplets fall at near terminal velocity. However, towards the conclusion of this investigation, the study team gained access to a laser precipitation monitor (LPM Model 5.4110.00.000 manufactured by Adolf Thies GmbH & Co, Germany) which enabled the team to critically review the Shelton *et al.* (1985) system. The LPM measures both the size and speed of individual droplets across ranges representative of natural rainfall. The generated droplet sizes and fall velocities during this investigation have been compared with those of natural rainfall (Marshall & Palmer 1948). The volumetric probability distributions $p(\phi)$ in each case are shown in figure 2 and are computed in a given droplet size range between diameters ϕ_1 and ϕ_2 as:

$$p(\phi_1 < \phi \leqslant \phi_2) = \frac{\displaystyle\int_{\phi_1}^{\phi_2} \phi'^3 n(\phi')\,\mathrm{d}\phi'}{\displaystyle\int_{0}^{\infty} \phi'^3 n(\phi')\,\mathrm{d}\phi'}. \tag{2.5}$$

The cumulative volumetric probability distributions $P(\phi)$ are also shown in figure 2 (computed using (2.5) with $\phi_1 = 0$ and $\phi_2 = (\phi)$ with the corresponding mean droplet velocities in each size range.

The principal disadvantage of using water jets as opposed to needle generators is the possibility of the droplet size distributions varying with changing rainfall rate. As shown in figure 2, there is a slight shift to larger drop sizes at the higher nozzle pressures and discharges except at the highest discharge condition. Under the conditions employed during this study (which mimicked Shelton *et al.* as closely as possible), the volumetric size distributions are similar in form to characterizations of natural rainfall at similar rain rates but with median droplet sizes approximately 67 % of that of real rainfall. There is a tendency for the nozzles to generate substantial amounts of mist ($\phi < 0.5$ mm) which resulted in the saturation of the corresponding LPM size/speed bins. Sensitivity testing showed that these large numbers of small particles make less than a few per cent difference to the size distributions shown in figure 2.

A disappointing outcome of the droplet speed measurements (figure 2*c*) is that the generation system yielded droplets falling at mean velocities substantially less than terminal.

As found by Tsimplis (1992), slicks on the tank surface can cause systematic drift in wave attenuation rates during testing. For approximately 1 h prior to testing each day during this study, any slick material was removed by mechanically generating steep waves, which carried any surface material to the downstream end of the tank by Lagrangian drift. A fan was used to ensure that any surface slick material was swept to and retained on the beach (figure 1). During testing, the tank surface was carefully monitored visually and at no time was the presence of slick material observed within the measurement area.

2.1. *Characterization of velocity fluctuations in the surface layer*

The near-surface velocity field generated by the rain was measured in the absence of any mechanically generated waves using a Sontek A827 side-looking 16 MHz, 5 cm focal distance, three-dimensional ADV with a measurement volume of 90 mm^3. For the most sensitive velocity measurements undertaken during this study, the ADV was mounted on a stationary structure that allowed the head to be positioned at different

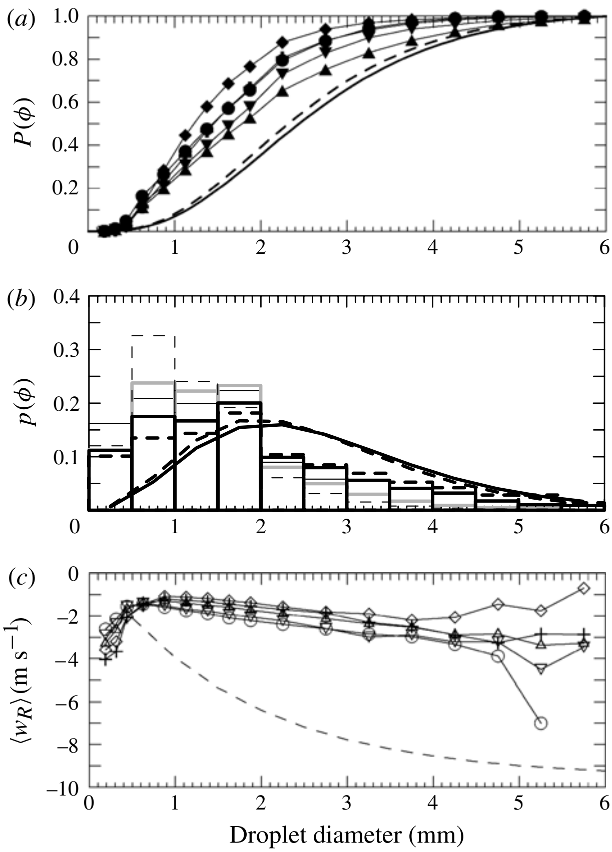

FIGURE 2. (a) Comparison of volumetric rainfall size cumulative distributions $P(\phi)$ (computed from (2.5)). The different symbols indicate the mean rain rate as follows: diamonds, 40 mm h^{-1}; circles, 76 mm h^{-1}; downward-pointing triangles, 108 mm h^{-1}; upward-pointing triangles, 141 mm h^{-1}; pluses, 170 mm h^{-1}. Size distributions for natural rainfall (Marshall & Palmer 1948) at intensities of 108 and 141 mm h^{-1} are indicated by thick dashed and thick solid curves respectively. (b) Comparison of volumetric rainfall size probability distributions $p(\phi)$ (2.5). The different line types indicate the mean rain rate as follows: dashed thin line, 40 mm h^{-1}; solid thin line, 76 mm h^{-1}; dashed thick line, 108 mm h^{-1}; solid thick line, 141 mm h^{-1}; solid grey line, 170 mm h^{-1}. Size distributions for natural rainfall (Marshall & Palmer 1948) at intensities of 108 and 141 mm h^{-1} are indicated by thick dashed and thick solid curves respectively. (c) Comparison of the mean fall velocity distributions $\langle w_R \rangle$. Corresponding fall (terminal) velocities of natural rainfall are indicated by the thin dashed line. The same symbols for the different rain rates have been used as in (a).

vertical levels so that only the head is immersed. The ADV measurement volume was projected away from its body and any supporting appurtenances so that the velocity measurements were taken beneath a sufficiently clear area of the surface that was freely irradiated with rain droplets (as shown in figure 1).

Assessment of turbulence spectra required propelling the ADV along the tank with its measurement volume located at shallow depths. It was found that puncturing the surface with the ADV during towing was undesirable so the alignment of the body of the ADV was changed so that it was submerged horizontally during towing with the measurement volume projected up towards the surface. The ADV body did generate a trailing wake when towing in this manner but it had no impact on the measurement point.

To maintain an ADV acoustic signal-to-noise ratio greater than 15 during the measurement period, the water column was seeded with a mixture of 10–30 μm diameter white Pliolite VT-ACL and rendering clay. The mixture was mixed initially over the entire depth. Testing showed that a delay prior to data recording of 5 min was adequate to ensure that the measurements were not contaminated by the initial seeding process or subsequent stirring. No visible settlement of the seeding material away from the air–water interface could be observed during this initial period or for the duration of the subsequent experiments. The ADV was checked before each measurement by standard beam monitoring procedures.

Preliminary static measurements showed that the near-surface fluctuating velocities generated by the rainfall were very small and that 31 mm was the minimum depth possible for reliable operation of the ADV under the rainfall conditions investigated. Consequently, for the static measurements, the ADV velocity range was set at its most sensitive level of $\pm 30\ \mathrm{mm\ s^{-1}}$. Measurement ensembles consisting of 163.84 s of 25 Hz velocity samples were used to characterize fluctuating velocities over a depth range between 31 and 151 mm. Studies by Voulgaris & Trowbridge (1998) have shown that accurate measurement of turbulence properties can be obtained from ADVs, provided that the geometric nature of the instrument and the underlying acoustic noise are properly recognized. The practical outcome of the factors in the present study was that the r.m.s. noise level was approximately 5 times greater for those velocity components measured parallel to the ADV head (v' and w' in figure 1) in comparison to the head-normal component (u'). Voulgaris & Trowbridge (1998) show that the ADV reliably measures the u' component directly provided that the turbulence levels are not too high.

Representative velocity spectra obtained from the static ADV measurements are shown in figure 3. Following Voulgaris & Trowbridge (1998) and Nikora & Goring (1998), the ambient acoustic noise level was determined directly from the measured velocity spectra and is clearly apparent above $45\ \mathrm{rad\ s^{-1}}$ in figure 3. The spectra shown in figure 3 also exhibit low-frequency ($<8\ \mathrm{rad\ s^{-1}}$) velocity fluctuations induced by seiches and other low-frequency motions within the tank itself. The intensities of velocity fluctuations induced directly by the rain were calculated by partitioning the spectra at the minimum spectral level at the lower frequencies and then deducting the acoustic noise from the remaining high-frequency spectrum. This process assumes that the instrument noise is uncorrelated with the velocity fluctuations (Bradshaw 1971).

Figure 4 shows the assembled fluctuating velocity profiles obtained from these measurements, in comparison with other studies. It can be observed that the r.m.s. magnitudes of v' and w' remain approximately 40 % higher than the comparable u' values as might be anticipated from figure 3 due to the higher acoustic noise that is difficult to remove with signal processing.

Measurements of turbulent dissipation rates are obtained conventionally by fitting the Kolmogorov model of the inertial subrange of the wavenumber spectrum (under the assumption of isotropic turbulence) where the inertial subrange is given by:

$$\Phi_{kt} = C_1' \varepsilon^{2/3} k_t^{-5/3} \tag{2.6}$$

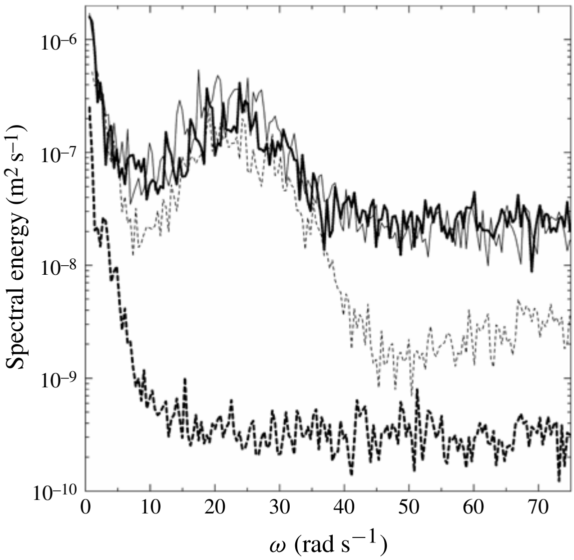

FIGURE 3. Representative fluctuating velocity spectra obtained from the acoustic Doppler velocimeter during the static measurements. $I = 141$ mm h^{-1}: u', light dashed line; v', heavy solid line; w', light solid line. No rainfall: u', heavy dashed line. Note the clearly defined minimum in spectral energy at approximately 8 rad s^{-1} in the rainfall measurement data and the approximately constant acoustic noise level above 45 rad s^{-1}. Note also the much lower acoustic noise of the head-normal velocity component and the approximately white spectrum in the absence of rainfall.

where Φ_{kt} is the wavenumber spectrum of the velocity fluctuations, $C_1' = 0.65$, ε is the turbulent kinetic energy dissipation rate per unit mass and k_t is the turbulent wavenumber (Pope 2000, p. 232).

Uniform vertical rainfall generates negligible mean flow. Thus the wavenumber spectrum measurement required profiling with the ADV towed along the tank at speed $U_{profile}$ as described earlier and by invoking Taylor's frozen turbulence hypothesis (where $U_{profile} \gg u'$, Tennekes & Lumley 1972, p. 253). A mean speed of $U_{profile} = 0.085$ m s^{-1} was used. The noise inherent in the measurements increased for two reasons:

(i) the ADV velocity range had to be increased to ± 300 mm s^{-1} thereby also increasing the system acoustic noise;

(ii) in spite of considerable care in the manufacture and operation of the trolley system, the along-tank jitter in the instrument package motion contaminated the measurements in the u'-direction.

The w'-velocity-component wavenumber spectrum exhibited the lowest noise level, with an approximately white spectral response in the absence of rainfall (figure 5).

For each measurement case, smoothed spectra were obtained by averaging four repeat measurements. The corresponding wavenumber spectrum in the presence of rainfall (with acoustic noise deducted) yielded an energy peak at the integral turbulence length scale l and a form of energy spectrum compatible with determining a dissipation rate. However, the estimated Taylor-scale Reynolds number (Re_λ, Pope 2000, p. 200) is less than 26 indicating the weakness of the fluctuating velocities and suggesting that a significant portion of the kinetic energy may be dissipated directly

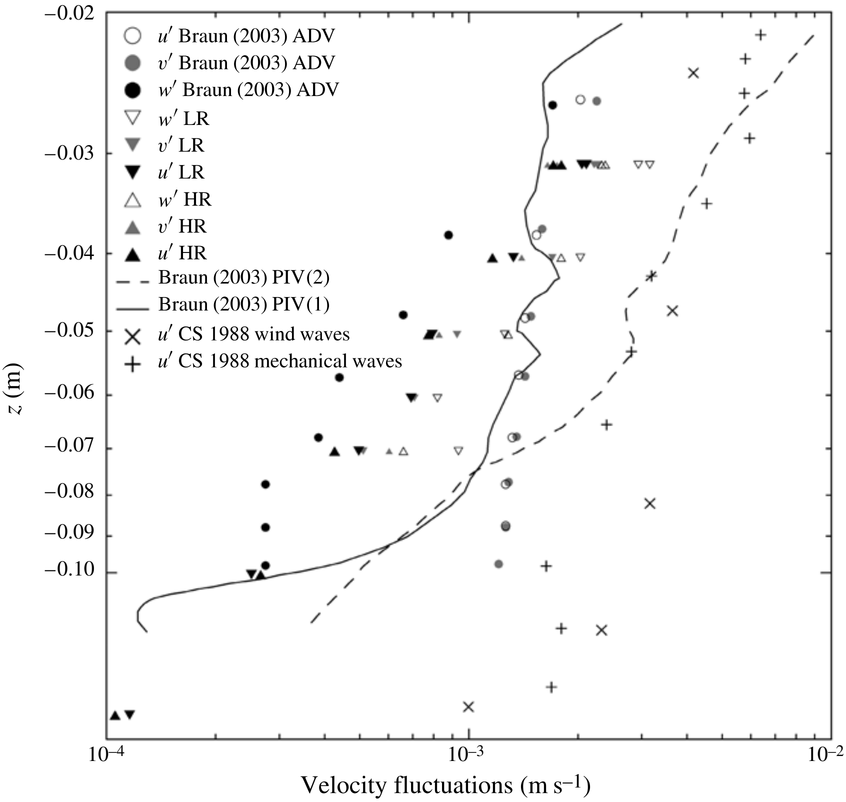

FIGURE 4. Vertical profiles of velocity fluctuations for both rainfall conditions of this investigation compared with other studies. Multiple identical symbols indicate repeat measurements. Present study: the two rainfall rates are indicated by downward-pointing triangles (108 mm h^{-1}) (LR) and upward-pointing triangles (141 mm h^{-1}) (HR). Note the close proximity of the v' and w' velocity components, indicating isotropy. ADV data of Braun (2003), shown as circles, are for 40 mm h^{-1}; note that the w' component has lower acoustic noise, and the proximity of u', v' measurements, indicating isotropy. PIV measurements of Braun (2003) show u': solid line (8 mm h^{-1}, 2.1 mm drop size); dashed line (216 mm h^{-1}, 2.9 mm drop size). The CS 1988 u' measurements are at lowest wind (1.7 m s^{-1}) for cases with no waves and wind-ruffled mechanical waves.

by viscosity. The spectrum is at the lower limit of the validity of Kolmogorov's assumptions, making it unsuitable for reliable determination of turbulent dissipation rates (Pope 2000, p. 235). The error in l was estimated from the upper and lower wavenumber values that encapsulate the peak of the spectrum (figure 5).

2.2. *Wave attenuation rate measurements*

The attenuation rates of monochromatic waves were measured for waves with frequencies between 10.5 and 21.0 rad s^{-1} and mean steepnesses (AK) ranging from 0.05 to 0.15. Wave generation commenced at least two minutes prior to data collection in each case. The ceiling value of $AK = 0.15$ was determined from preliminary observations in the absence of rainfall that wave breaking occurred due to Benjamin–Feir instabilities within the test section (Benjamin & Feir 1967). Wave

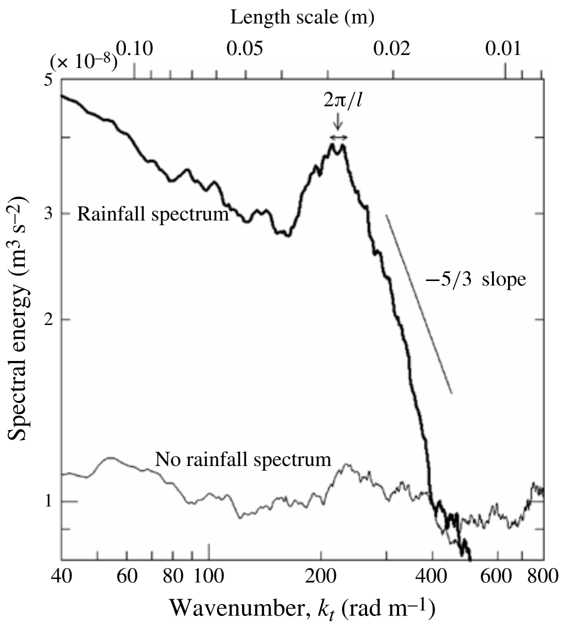

FIGURE 5. Representative wavenumber spectra obtained from the towing trolley experiments for the w' velocity component (ADV mounted at 37 mm depth). Plotted spectra are the mean of 4 independent measurements, smoothed with 11 point bin averages. Light line shows the spectrum obtained in the absence of rainfall and shows little modulation with wavenumber. Heavy line shows values for $I = 141$ mm h^{-1} without the acoustic noise deducted. A line with $-5/3$ slope is shown as a reference. The integral length scale (l) for $I = 141$ mm h^{-1} is indicated by the arrow and its uncertainty by the double-headed arrow. Note the higher noise levels in comparison with the static measurements shown in figure 3.

attenuation rates in the absence of rain were measured to obtain the background viscous attenuation within the test facility.

Wave attenuation along the tank was monitored by four pairs of capacitance probes located along the tank at fetches 1.60, 6.00, 10.35 and 16.80 m from the wave paddle (figure 1). Each probe was calibrated at least twice before and after the measurements and showed gain stability better than ± 2 %. The capacitance wave probe noise levels at the sampling rate for static conditions had a standard deviation less than 0.05 mm. Raw data were captured at a 600 Hz sample rate per channel for 102.4 s by a National Instruments PCI-6225 data acquisition card fitted to a conventional personal computer. These data were averaged using 15-point bins to obtain a net sampling rate of 40 Hz prior to spectral processing.

Fast Fourier transform (FFT) techniques were used to compute the energy characteristic of the monochromatic waves from each water level time series. The high digitization rate coupled with the large FFT sample size enabled excellent resolution and extraction of the monochromatic wave energy. Representative spectra obtained both in the presence and absence of rain are shown in figure 6. The spectral energy of the monochromatic waves can be distinguished clearly from the gravity–capillary energy of waves generated by the rain. In the absence of rain, the nonlinear harmonics of the fundamental wave are clearly apparent in these spectra, highlighting the low noise characteristics of the wave probes. The energy associated with a monochromatic

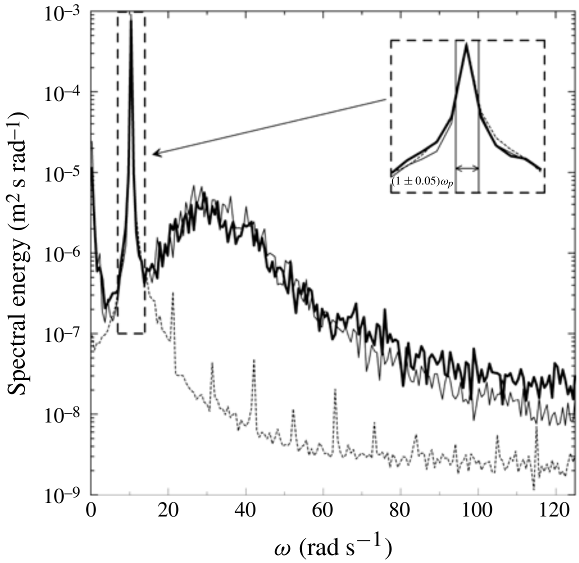

FIGURE 6. A set of representative wave spectra for the test case $\omega = 10.46\ \mathrm{rad\ s^{-1}}$, $AK = 0.05$ and recorded at a distance of 10.35 m from the wave generator. No rainfall, dashed line; $108\ \mathrm{mm\ h^{-1}}$, solid thin line; $141\ \mathrm{mm\ h^{-1}}$, solid thick line. Note the clearly defined harmonic peaks in the spectrum obtained in the absence of rainfall. The inset indicates the frequency region used to characterize local monochromatic wave energy.

wave of angular frequency ω_p was extracted from each record by integrating the spectral energy within the angular frequency band $(1 \pm 0.05)\omega_p$.

Figure 7 shows the decline in monochromatic wave energy with fetch for waves of angular frequency $15.7\ \mathrm{rad\ s^{-1}}$ and varying wave steepnesses for a rainfall rate of $141\ \mathrm{mm\ h^{-1}}$. For each experiment, the total wave attenuation coefficient (1.4), Δ_T, was determined by a least-squares fit to the data and 90 % confidence limits determined according the method described by Peirson *et al.* (2003), p. 354. It was observed that the correlation coefficient decreased systematically with decreasing wave frequency as a consequence of the lower attenuation rates. The measurement results are discussed in the next section.

3. Results and discussion

3.1. *Rain-generated wave spectra*

The measurements of the rain-generated waves, in the presence and absence of the mechanically generated waves, are compared with those obtained by Bliven *et al.* (1997) in figure 8. It should be noted that capacitance probes are not ideal for such measurements due to the potential for surface tension effects and local sheltering of the surface by the probe elements. During subsequent testing, we added the small probe rain shelters shown in figure 1 to minimize the incidence of water ingress into the wave electronics. It was found that the addition of the rain shelters attenuated the measured rain-generated spectra relative to the original measurements. Spectra obtained from the original measurements are shown in figure 8 in comparison with those of Bliven *et al.* (1997). The spectral bandwidths and peak wave frequencies found during the present study are very similar to those measured by Bliven *et al.*

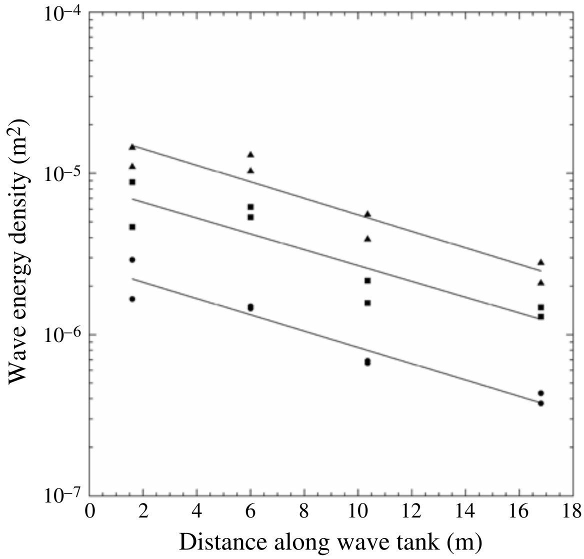

FIGURE 7. Wave energy as a function of distance from the wavemaker for $I = 141$ mm h^{-1} with $\omega = 15.7$ rad s^{-1}: circles, $AK = 0.05$; squares, $AK = 0.10$; triangles, $AK = 0.15$. Lines show the exponential best fits used to determine attenuation rate.

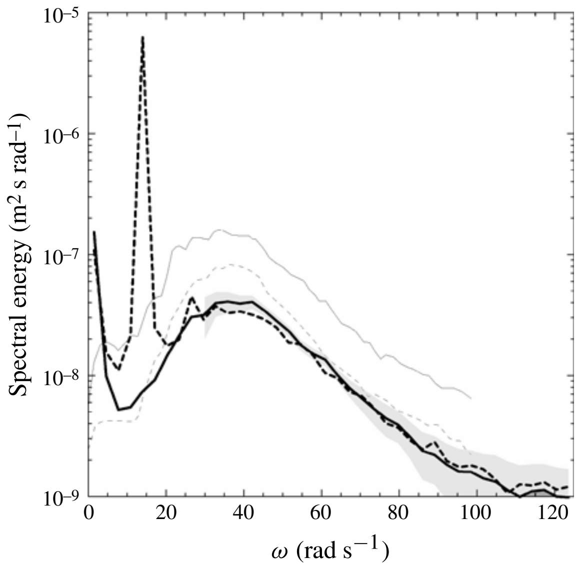

FIGURE 8. Rain wave spectrum in the absence of monochromatic waves: present study, 108 mm h^{-1} heavy solid line; Bliven *et al.* (1997): 50 mm h^{-1} thin dashed line, 200 mm h^{-1} thin solid line. Rain wave spectrum in the presence of monochromatic waves (present study): heavy dashed line $\omega = 14.0$ rad s^{-1}, $AK = 0.05$, 108 mm h^{-1}. Data were obtained with the minimal surface sheltering possible with our probes. The grey area shows the confidence interval given by the standard statistical error from all wave rain spectra for all wave scenarios tested under the 108 mm h^{-1} condition. Note that no significant difference can be observed between the rain wave spectra at frequencies above 30 rad s^{-1} in the absence and presence of the monochromatic waves.

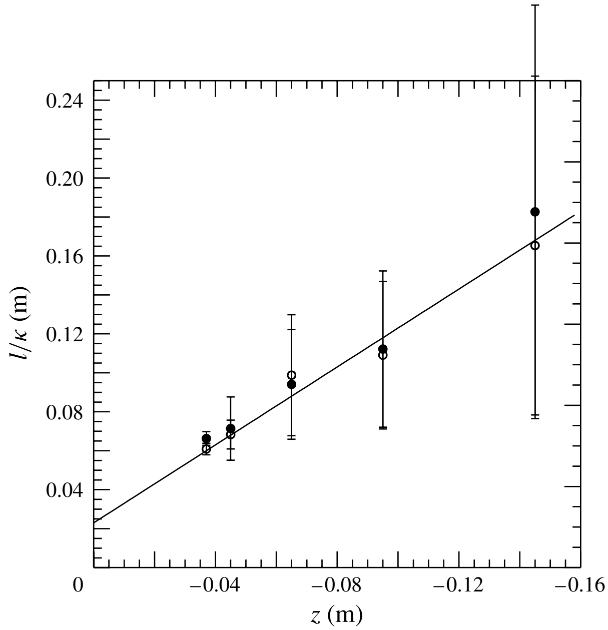

FIGURE 9. Vertical profile of the fluctuating velocity integral length (l) obtained from the wavenumber spectra. The solid line shows a linear fit with a slope of unity. Open circles, $I = 108$ mm h^{-1}; solid circles, $I = 141$ mm h^{-1}.

For the rainfall rates tested, no significant difference between the wave spectra was observed, but predictions based on Bliven *et al.* (1997) indicated that only a 17 % difference in total spectral energy for the two test cases would be anticipated. However, these present observations reveal that the rain-generated waves are insensitive to the underlying wave field. Two full spectra from the present measurements are shown: the rain-generated spectrum obtained for $I = 141$ mm h^{-1} in the absence of monochromatic waves and the same condition but with added monochromatic waves of frequency 14.0 rad s^{-1} and mean steepness 0.05. The scatter in all data sets is indicated by the grey shaded region in figure 8. The variance of the spectra remains less than 20 % for frequencies less than 80 rad s^{-1}. While this result is likely to be robust when there is strong separation of the time scales of the rain-generated and underlying gravity waves, this may not be the case when the frequency of the underlying waves approaches that of the rain-generated waves (Peirson & Garcia 2008).

3.2. *Characteristic fluctuating velocity length scales*

The fluctuating velocity intensities were found to be very weak, making it impossible to infer dissipation rates based on conventional approaches to turbulence. However, the spectra did yield systematic values of an integral length scale (as shown in figure 5). The integral length scales were extracted from the measured spectra and are summarized in figure 9. Integral length scales were anticipated to conform to wall-layer form (e.g. Craig & Banner 1994):

$$l = \kappa(z_0 + |z|), \tag{3.1}$$

where κ is the von Kármán parameter ($=0.40$), z_0 is the roughness length on the water side and z is the vertical coordinate measured positive upwards from the mean water level.

Figure 9 shows variation of l/κ as a function of z from which a value of z_0 of 23 mm can be determined. This value is qualitatively consistent with the visualization images of Lange, van der Graaf & Gade (2000) who show that turbulence initiated by a single drop occurs via the formation of vortex rings at an approximate depth of 20 mm. The condition is also comparable to the turbulent dissipation balancing diffusion model developed by Craig & Banner (1994). Unfortunately, the weakness of the fluctuating velocities makes it impossible to compare quantitatively the present data with the Craig & Banner (1994) model which assumes a well-developed inertial subrange (2.6).

Rain-irradiated surfaces are characterized by chaotic behaviour associated with both the rain ring waves and turbulent motions. Under wind-forced conditions, CS 1988 found that they were not able to distinguish the high-frequency ripples and near-surface turbulent motions, and that these played a combined role in the formation of the Reynolds stress mediating the total downward wind-induced momentum flux. Csanady (1990) coined the term 'wavulence' to describe such complex surface motions. Estimates of the potential contribution of the ring waves to the fluctuating velocities based on the most energetic rain spectrum measured by Bliven *et al.* (1997) indicated that these wave motions could potentially contribute approximately 50 % of the measured fluctuating velocities at 31 mm depth, reducing to a potential 30 % contribution at 62 mm depth.

3.3. *Fluctuating velocities*

Profiles of the fluctuating velocities are shown in figure 4 in comparison with data measured by Braun (2003). The lowest-noise velocity components in figure 4 were u' for the present study and w' during Braun's study. The consistency of the two sets of results is remarkable given the significantly different tank configurations, rainfall rates, generation methods and consequent rain energy flux. We could find no systematic change in fluctuating velocity intensity by changing the rainfall rate. Braun (2003) found an almost identical decay in fluctuating velocity intensity with depth although the intensities were approximately 75 % of those found in this study. The apparent insensitivity of the fluctuating velocities to the rainfall intensity is striking.

Although the velocities recorded in the head-parallel directions are more subject to acoustic noise (and therefore show higher apparent fluctuating velocity intensity in these directions), the head-parallel data of both Braun and the present study confirm a significant result: the near-equivalence of these orthogonal measured fluctuating velocities shows isotropy at all practical measurement depths. In her study, Braun does not appear to address the issue of ADV acoustic noise, which may be the reason for the more rapid divergence of her head-normal and head-parallel velocity component intensities.

As a sensitivity test on the present results, we examined the variation in u' as a function of rainfall rate while maintaining the ADV measurement point at a fixed depth of 31 mm. As shown in figure 10, no systematic trend in the fluctuating velocity intensities could be detected over the range of rainfall rates that could be generated with this facility.

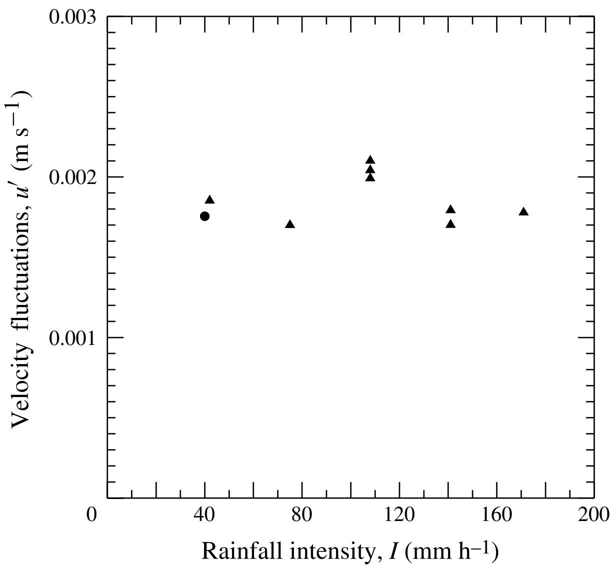

FIGURE 10. Velocity fluctuations recorded at constant depth of 31 mm showing the relative insensitivity to rainfall intensity. Triangles, u' present study at depth = 31 mm; solid circle, w' Braun (2003, interpolated). Note that present study data were obtained with rainfall rates outside the operating range recommended by Shelton *et al.* (1985) and achieved by adjusting the water and air flow rate to produce an approximately uniform rainfall rate.

3.4. *Wave attenuation rates in the presence of rain*

To determine the wave attenuation coefficient due to rainfall, Δ_R, from (1.3), analytical expressions for the viscous attenuation coefficient Δ_v for a clean surface (Van Dorn 1966; Dore 1978) were compared with wave decay rates in the absence of rain (figure 11). (We note errors, by our assessment probably typographical, in expressions of Van Dorn (1966, clean mobile surface expression, p. 770), Wilson *et al.* (1973, equation (6)) and Mitsuyasu & Honda (1982, equation (6))). Shown also is the Van Dorn (1966) Δ_v characterization of immobile surfaces. The clean-surface expressions for Δ_v in deep water include both surface (Δ_s) and wall (Δ_w) components:

$$\Delta_v = \Delta_s + \Delta_w. \tag{3.2}$$

The surface term has the following water-side and air-side contributions:

$$\Delta_s = \frac{4\nu k^2}{c_g} + \sqrt{8\left(\frac{\rho_{air}\mu_{air}k^2\omega}{\rho^2 c_g^2}\right)}, \tag{3.3}$$

where ρ_{air} and μ_{air} are the density and absolute viscosity of air, and:

$$\Delta_w = \frac{4k}{b_t}\left(\frac{\nu}{2\omega}\right)^{1/2} \tag{3.4}$$

where b_t is the tank width.

The results of Wilson *et al.* (1973) were well-predicted by these expressions for conditions of very low wave steepness ($AK < 0.02$). Mitsuyasu & Honda (1982) found reasonable consistency between small-amplitude predictions and their measured results, but found that there was a systematic finite-amplitude effect. In the present

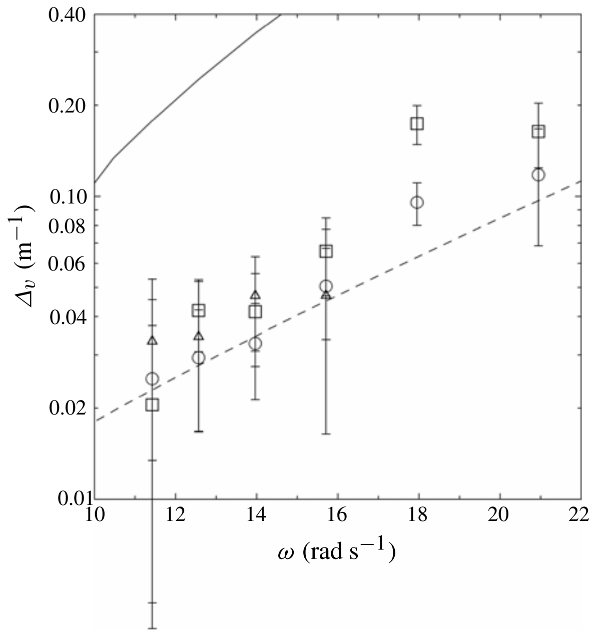

FIGURE 11. Spatial attenuation coefficient in the absence of rainfall as a function of wave frequency and mean steepness. Symbols indicate mean steepness as follows: triangles, $AK = 0.05$; circles, $AK = 0.10$; squares, $AK = 0.15$. Theoretical predictions: dashed line, clean surface (3.2); solid line, Van Dorn (1966) fully contaminated surface.

study, values computed from (3.2) form a systematic lower bound to the measured values of the attenuation coefficient (figure 11). The attenuation rates at $AK = 0.15$ are systematically higher by a factor of 1.44 ± 0.22 than the corresponding rate measured at $AK = 0.10$, and the attenuation rates at higher frequency diverge from small amplitude theory. These findings may provide a route for resolving the finite-amplitude viscous effects observed by Banner & Peirson (2007) and Tian *et al.* (2010). Consequently, the analytical expressions were not used and the attenuation coefficients due to rainfall alone were determined by deducting the measured attenuation rates in the absence of rainfall.

In figure 12, the rainfall-induced attenuation rates measured during the present study are shown as a function of wave frequency in comparison with the measurements of Tsimplis (1992) and Poon *et al.* (1992). No systematic difference in attenuation rate can be observed between the different rainfall rates, consistent with the findings of Tsimplis (1992) and Poon *et al.* (1992). To our knowledge, a threshold rainfall rate or rainfall kinetic energy below which attenuation rate varies with rainfall rate remains to be identified.

Attenuation rate appears insensitive to wave steepness, consistent with Tsimplis (1992), but the attenuation rates determined by the two 1992 and present studies are all significantly different (figure 12). The attenuation rates of this investigation form a systematic upper envelope to the Tsimplis data, which may be indicative of contamination issues during his study (Tsimplis 1992, p. 408). The Poon *et al.* data show very weak frequency dependence in comparison with the other data and agreement with the present study at higher frequencies but, at an angular wave frequency of ∼11 rad s^{-1}, the Poon *et al.* (1992) measured attenuation rates are an order of magnitude higher than those measured here.

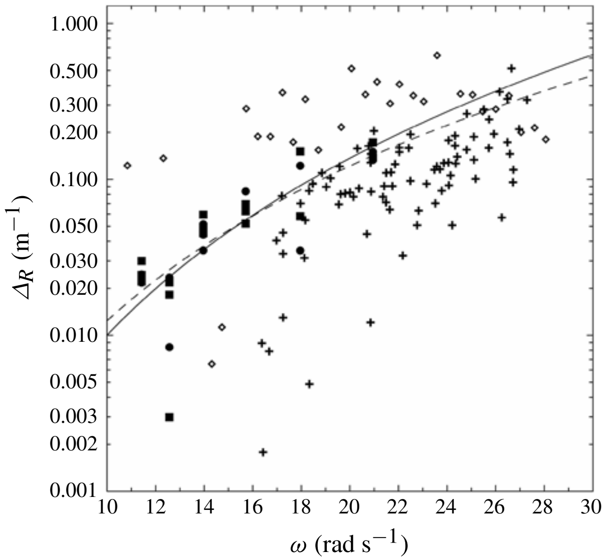

FIGURE 12. Comparison of wave attenuation coefficient due to rainfall: plus signs, Tsimplis (1992); open diamonds, Poon *et al.* (1992) (excluding data points showing weak growth). Present study: solid circles, 108 mm h^{-1}; solid squares, 141 mm h^{-1}. Present study best-fit curves determined by the least-squares techniques: dashed line ($\Delta_R = 6.2 \times 10^{-6}\omega^{3.30}$), 108 mm h^{-1}; solid line ($\Delta_R = 1.7 \times 10^{-6}\omega^{3.77}$), 141 mm h^{-1}.

Investigation	Eddy viscosity (m^2 s^{-1})
Tsimplis (1992)	$3.43 \times 10^{-6} \pm 0.19 \times 10^{-6}$
Poon *et al.* (1992)	1.20×10^{-5}
This study	$8.56 \times 10^{-6} \pm 0.58 \times 10^{-6}$

TABLE 2. Eddy viscosities in the presence of rainfall.

The insensitivity of wave attenuation rates to rainfall rate observed in each data set allows the results to be summarized in terms of an eddy viscosity (1.2). Although Tsimplis (1992) reported an eddy viscosity value of 30×10^{-6} m^2 s^{-1}, recalculation using his wave attenuation coefficients (figure 12) yields an eddy viscosity 10 times smaller. A comparison of the eddy viscosity values of this study with Poon *et al.* (1992) and the recalculated Tsimplis (1992) values is shown in table 2.

3.5. *Near-surface energy fluxes*

The enigma of insensitivity of wave attenuation rate to rainfall rate seems to be linked to the apparent insensitivity of the subsurface fluctuating velocities to the rainfall condition. However, theoretical studies (e.g. Manton 1973; Houk & Green 1976; Nystuen 1990; Craeye & Schlüssel 1998) have continued to assume that there is a direct transfer from rainfall kinetic energy flux into turbulent motions beneath the air–water interface. This is not the case and significant dissipation occurs in the vicinity of the open water surface.

For the present experiments, an approximate energy budget can be composed as follows.

(i) The net horizontal mean fluxes of wave and turbulent energy are assumed zero.

(ii) An estimated total subsurface turbulence dissipation rate ($\dot{E}_{turb\_diss}$) was determined from the measured fluctuating velocity profiles (figure 4):

$$\dot{E}_{turb\_diss} = -\int_{z_0}^{\infty} \rho\, \varepsilon(z)\, \mathrm{d}z, \tag{3.5}$$

where the local dissipation is given by:

$$\varepsilon(z) = A\frac{u'(z)^3}{l(z)}, \tag{3.6}$$

where $A = 3$ (Burattini, Lavoie & Antonia 2005, figure 3, an assumed overestimate based on a Reynolds number of 26).

(iii) The total surface viscous and rain attenuation rates of the rain-generated waves was obtained via:

$$\dot{E} = -\int c_g(\omega)\Delta_T(\omega)E(\omega)\, \mathrm{d}\omega, \tag{3.7}$$

where the dissipation of the rain-generated waves has been determined using (1.3) and (3.2) with the fitted expressions developed from the data in figure 12.

For the present experiments, the rainfall kinetic energy fluxes are of order 0.1 W m^{-2} which is significantly greater than the sum of estimated subsurface turbulent dissipation (0.003 W m^{-2}) and the total attenuation rates of the rain-generated waves (0.03 W m^{-2}).

For possible explanations of these high interfacial dissipations, we turn to the extensive literature on droplet and splash behaviour (e.g. Prosperetti & Oguz 1993; Yarin 2006). This area of fluid mechanics has proven challenging to those compiling energy budgets even for individual droplets. Energy assessment seems to have been largely restricted to the approximately irrotational period prior to surface rupture (e.g. Fedorchenko & Wang 2004; Gordillo & Gekle 2010).

The fluid mechanical behaviour of drops impacting water surfaces is characterized by two key non-dimensional parameters (Fedorchenko & Wang 2004): a Weber number (2.3) and a Froude number:

$$F = \frac{w_R^2}{g\phi}. \tag{3.8}$$

Craeye & Schlüssel (1998) reported a theoretical analysis based on published characterizations of rainfall-generated surface craters to determine surface turnover time for the purposes of determining constituent exchange. Their work provides a very useful perspective. Assuming a threshold value of $W = 10$ for droplet puncture of the surface and integrating their equation (1) numerically using their expressions (2)–(4) yields the turnover time scale shown in figure 13 as a grey dotted line. We can superimpose on this curve a sequence of characteristic rainfall rates and time scales.

The photographs of Fedorchenko & Wang (2004) show characteristic cycle times associated with droplet impingement of order 0.125 s (for example, their figure 1). The analysis of the initial ring waves generated by rain droplets of Le Méhauté (1988) yields initial characteristic time scales of order 0.3 s. The implication is that, for the

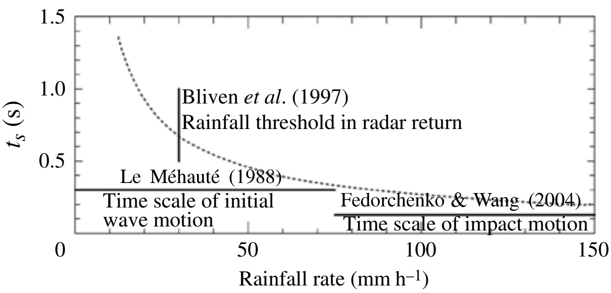

FIGURE 13. Surface renewal time for natural rainfall as a function of rainfall rate with the expression of Craeye & Schlüssel (1998) shown as a grey dotted line. Solid lines indicate characteristic rainfall rates or time scales associated with rain impacting water surfaces determined by the authors indicated.

present study, as the rainfall rate increases, incoming droplets directly impact surface perturbations generated by immediately preceding impacts.

Leneweit *et al.* (2005) and Okawa, Shiraishi & Mori (2008) have investigated the influence of approach angle on the surface motions generated by impinging individual droplets on undisturbed water surfaces. They found that as the angle between the approaching droplet and the surface normal increases, a series of transitions in surface behaviour are observed and a Weber number based on the drop velocity normal to the surface becomes the characteristic scale. At modest angles between the droplet approach direction and the surface normal, greater levels of spallation are observed. At highly oblique approach angles, reduced immersion of the incident drop volume is observed with possible ricochet of the incident drop.

As a surface becomes increasingly disturbed, droplet–surface interactions become much more complicated due to increased interactions between incoming droplets and a variety of rapid vertical wave motions. Note that the time scale shown in figure 13 represents surface turnover at a surface point, not that within the inscribed area of a finite droplet. For finite droplets, the characteristic time scale of contact with a surface strongly perturbed by a preceding localized impact would be considerably less than Craeye & Schlussel's renewal time scale.

This provides an alternative perspective on high-rainfall-rate-impacted water surfaces: the interface is not undisturbed. Rather it is characterized by continuously interacting violent surface motions, bubble injections and ejections as well as (presumably) ejections of spallated droplets across moving surfaces with localized areas of very steep slope.

This overall picture provides the basis for a qualitatively plausible explanation of the insensitivity of the present experiments to rainfall rate. Above a rainfall rate in the vicinity of 30 mm h^{-1}, increasing the rainfall rates may merely increase the frequency of ricocheting or spallation motions with negligible increase in deeply penetrating vertical droplet motions.

Figure 13 indicates a possible threshold in rainfall intensity at terminal velocity for transition between the different regimes of rainfall enhancing or saturated behaviour. This is in reasonable agreement with the threshold identified by Bliven *et al.* (1997) of significantly attenuated responses in the surface wave field energy and radar backscatter above a rainfall rate of approximately 30 mm h^{-1}, also indicated in figure 13. Characteristic time scales obtained from Le Méhauté (1988) and Fedorchenko & Wang (2004) are also shown.

Le Méhauté & Khangaonkar (1990) developed a predictive momentum-based model for wave attenuation due to rainfall. Can the present data be used with their model to predict this rainfall threshold? Using the appropriate value from table 2, equating (1.1) and (1.2) and assuming a wavenumber characteristic of the present study of about 30 m^{-1}, such decay is anticipated to be induced by a rainfall rate of over 1000 mm h^{-1}. This result highlights the minor role that (vertical) rain momentum flux is predicted to play in comparison with the wave-attenuating momentum fluxes generated by the surface fluctuating motions.

A possible reconciliation of the present observations and near-surface measurements of turbulent dissipation by Zappa *et al.* (2009) is also noted. Zappa *et al.* observed that near-surface dissipation systematically increased with rainfall up to rates of 50 mm h^{-1}. It is anticipated that a turbulent dissipation ceiling would be observed if their observations were suitably extended to higher rainfall rates.

The present findings may inform other disciplines that rely on high rainfall rates to determine surface responses at much lower levels of forcing (industrial processing, hydrology and agriculture, for example). If a surface water layer is present, interaction between droplets and the water surface motion will be suppressed at lower rainfall rates but significant nonlinear dissipation is anticipated to develop above a threshold surface turnover frequency.

To overcome the insensitivities of previous studies and observe a response in wave attenuation rate to rainfall rate, it appears that much lighter rainfall rates will be required. Sufficiently lower rainfall rates are predicted to yield lower wave attenuation rates, implying the need either for error reduction or increased fetch investigation lengths. Fabrication of suitably large rainfall generation equipment will be an expensive activity.

3.6. *Comparison with other wave attenuation processes*

These quantified attenuation rates due to rainfall can be compared with other processes known to attenuate surface waves. For comparison, we quantify non-dimensional temporal attenuation rate as $(1/\omega E)(\mathrm{d}E/\mathrm{d}t)$ and present it as a function of wave frequency as shown in figure 14.

There are five processes for which we were able to find quantifiable wave attenuation data in the literature, namely, molecular viscous damping, wave breaking, subsurface turbulence, opposing wind and rainfall, the subject of the present study. These data are summarized in figure 14 and are discussed briefly in turn.

Viscosity

A complete expression (3.3) that incorporates attenuation due to the water and air viscosities at the free surface has been included in figure 14. At high frequencies, the water viscosity dominates the surface viscous attenuation rates and increases as ω^3 but at lower frequencies the air-side behaviour becomes increasingly important (Collard, Ardhuin & Chapron 2009).

Deep-water wave breaking

Deep-water breaking is a highly nonlinear wave attenuation process. Below a threshold in the local surface energy density convergence rate, breaking does not occur. Above this threshold, strong energy fluxes develop rapidly that result in dissipation of excess wave energy flux through breaking (Duncan 1981; Rapp & Melville 1990; Banner & Peirson 2007). Breaking strength is conventionally characterized by a

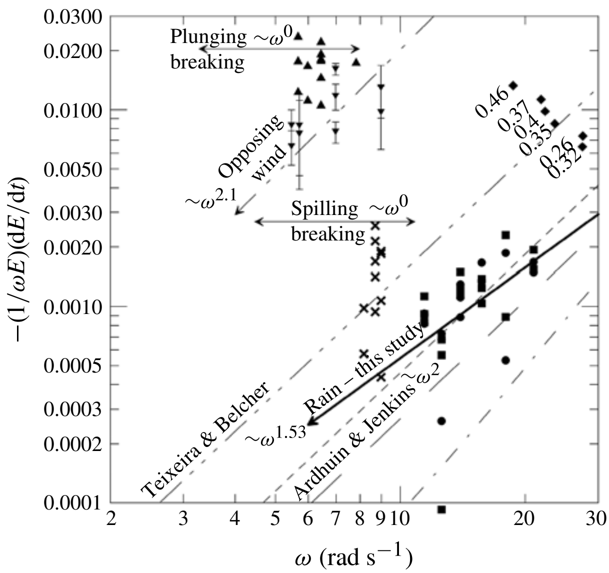

FIGURE 14. Wave attenuation rates. Viscous attenuation: dash-dot line, (1.2) and (3.3). Deep-water wave breaking: crosses, Banner & Peirson (2007); upward pointing triangles, Tian *et al.* (2010). Opposing wind: downward pointing triangles, Peirson *et al.* (2003) $\hat{u}_*^a = 0.32\ \mathrm{m\ s^{-1}}$; dash-double-dot line, Peirson *et al.* (2003) equation (11) $\hat{u}_*^a = 0.32\ \mathrm{m\ s^{-1}}$ $AK = 0.1$. Rainfall (present study): solid circles, 108 mm $\mathrm{h^{-1}}$; solid squares, 141 mm $\mathrm{h^{-1}}$; solid line, best least-squares fit; short dashed line, best fit assuming ω^2 dependence. Wave energy loss in the presence of wind: diamonds, Peirson & Banner (2000) – adjacent values indicate $\hat{u}_*^a$; dash-triple-dot line, TB (2002) with $\hat{u}_*^a = 0.32\ \mathrm{m\ s^{-1}}$, long-dash line, AJ (2006). Note the data assembly for this figure has been made in terms of a value of $\hat{u}_*^a = 0.32\ \mathrm{m\ s^{-1}}$ for comparison purposes.

coefficient b in an expression developed by Duncan (1981):

$$\varepsilon_L = \frac{b\rho c_{break}^5}{g} \tag{3.9}$$

where ε_L is the breaking energy loss rate per unit length and c_{break} is the speed of the breaking front.

In figure 14, we have summarized the deep-water breaking attenuation rates presented by Banner & Peirson (2007) for spilling breakers and Tian *et al.* (2010) for plunging breakers. This has been accomplished by extracting the energy lost through the breaking process that is in excess of losses attributable to viscosity (Banner & Peirson 2007, figure 6) to form a spatial attenuation rate over a distance X_{AB}, the swept distance of the actively breaking front. Tian *et al.* (2010) carefully documented the quantity X_{AB} for plunging breaking conditions.

Using the linear dispersion relation to transform wave speed to an equivalent frequency, (3.9) becomes:

$$\frac{1}{\omega E}\frac{\mathrm{d}E}{\mathrm{d}t} = \frac{b}{k^2\langle\eta^2\rangle k X_{AB}}, \tag{3.10}$$

yielding no frequency dependence of the breaking process in Duncan's form for waves of the same geometric aspect and behaviour.

The present results highlight the differences in energy loss between spilling and plunging breaking in deep water: plunging breaking exhibits normalized loss rates that are approximately one order of magnitude higher than spilling waves.

By constructing a surface momentum flux budget for actively wind-forced breaking microscale waves, Peirson & Banner (2000) were able to quantify the corresponding energy fluxes from the wave field. Their normalized results are shown in figure 14 and annotated with the corresponding wind-induced surface friction velocity. The Peirson & Banner (2000) results sit significantly higher in figure 14 than would be predicted by considering spilling breaking losses alone. This suggests additional loss from these small-scale wave fields due to wave–wind turbulence interactions or viscous losses due to attendant parasitic capillary waves (Longuet-Higgins 1994).

Wave–turbulence interactions

Whereas wave attenuation has been associated with a surface horizontal momentum flux (usually, wind), attenuation rate is conventionally expressed in the form (Belcher & Hunt 1998):

$$\frac{1}{\omega E}\frac{\mathrm{d}E}{\mathrm{d}t} = \beta \frac{\rho_a}{\rho}\left(\frac{\hat{u}_*^a}{c}\right)^2, \tag{3.11}$$

where $\hat{u}_*^a$ is the air-side friction velocity, ρ_a is the density of the air, c is the (assumed) linear wave speed and β is a non-dimensional growth or attenuation coefficient.

Assuming a relationship between the wind-generated friction velocity and near-surface turbulence intensity obtained from MT 1995, TB 2002 determined an attenuation coefficient $\beta = -0.8$ in the presence of wind while AJ 2006 yields $\beta = -2$. Assuming a friction velocity $\hat{u}_*^a = 0.32\ \mathrm{m\ s^{-1}}$, the TB 2002 equation (3.24) and the corresponding AJ 2006 curve are both shown in figure 14.

Opposing wind

Peirson *et al.* (2003) quantified the attenuation rates of waves due to an opposing wind under laboratory conditions and found very strong levels of wave attenuation. Their equation (11) with $AK = 0.1$ is shown in figure 14 with selected data for $\hat{u}_*^a = 0.32\ \mathrm{m\ s^{-1}}$. The present results show that opposing wind is a strong process under laboratory conditions even in comparison with local breaking.

Rainfall

In figure 14, the data gathered during this investigation have been non-dimensionalized via (1.2) and show similar frequency dependence to the TB 2002/AJ 2006 formulations. Rainfall is now ranked in the context of other identified wave attenuation processes.

Comparison between rainfall attenuation rates and the TB 2002 formulation requires specification of a representative friction velocity or turbulent intensity in proximity to the free surface. For the Hunt–Graham profile, subsurface turbulence is characterized by a representative value that occurs well away from the surface. In the present investigation, no such value exists. For wind-forced waves, the fluctuating velocity intensities also systematically decrease with depth as shown in figure 4 (see also, CS 1988 and MT 1995). Significant near-surface anisotropy in the fluctuating velocities was observed during these wind-forced wave investigations, in contrast with the present investigation.

Given the conventional use of (3.9), it is potentially useful to examine whether the observed attenuation of waves by rain can be characterized in terms of a non-dimensional attenuation coefficient β. TB 2002 ssume a characteristic turbulent velocity associated with wave attenuation that is three times the wind-induced friction velocity by appealing to MT 1995 (presumably, p. 323). That is,

$$\widehat{u}' = 3\hat{u}_*^w, \tag{3.12}$$

$\hat{u}_*^w$ being the water-side friction velocity and assuming equal momentum fluxes on both sides of the interface, that is:

$$\rho \hat{u}_*^{w^2} = \rho_a \hat{u}_*^{a^2}. \tag{3.13}$$

As there is no externally applied horizontal momentum flux, a characteristic friction velocity must be inferred to determine the parameter β in (3.11). For rainfall attenuation, there are three potential methods to determine appropriate values of $\widehat{u}'$ (and by implication $\hat{u}_*^a$ and $\hat{u}_*^w$). These are discussed in turn.

(i) Rain kinetic energy flux to the free surface

Green & Houk (1979) determined a value of friction velocity via:

$$\dot{E}_{rain} = \rho \hat{u}_*^{w^3}. \tag{3.14}$$

As previously discussed, both wave attenuation rates and subsurface fluctuating velocities show weak dependence on rain kinetic energy flux and (3.14) is unlikely to form a suitable basis for characterizing wave attenuation rates. For the rainfall conditions of the present study, (3.14) yields values of $\hat{u}_*^w$ in the vicinity of 0.05 m s^{-1} implying a value of $\beta = O(0.23)$.

(ii) Boundary layer characterization

Given that the source of the water column forcing is adjacent to the interface, it would be appropriate to select a scaling value characteristic of the surface generation process. The raindrop visualization studies of Green & Houk (1979) and Braun (2003) and the present roughness length measurements indicate a source of fluctuating velocities in the vicinity of 23 mm depth. Consequently, we have extrapolated the measured fluctuating velocity intensities to this level to obtain the scaling velocity $\widehat{u}'(=0.0033$ m s$^{-1})$. Using the equivalent value of $\hat{u}_*^a$ (equations (3.12) and (3.13)), yields a value of of $\beta = O(400)$. This highlights the very strong destructive coupling between the waves and the fluctuating motions in comparison with rates of wave growth due to wind.

(iii) Normalization of fluctuating velocity intensity profiles

As shown in figure 4, the fluctuating velocity profiles in the water determined during the present study and those obtained by CS 1988 at their lowest wind speed show similar depth variations (while noting that the surface conditions of the two studies are significantly different: the surface conditions of CS 1988 would have been relatively smooth, while in this study, the surface is disrupted violently by the impinging raindrops).

Assuming that the two sets of profiles can be normalized by a value of $\hat{u}_*^w$ to yield the same non-dimensional profile, this profile can be determined from the values of $\hat{u}_*^w$ measured by CS 1988. The corresponding value of $\hat{u}_*^w$ required to match the rainfall data to the non-dimensional profile is 0.00012 m s^{-1}. This implies an even higher value of β than given by the boundary layer comparison.

In summary, although wave attenuation processes can now be assembled into a hierarchy such as that shown in figure 14, presently available quantitative methods of forming inter-relationships between them remain extremely poor. The primary reason for this is that a quantitative fundamental understanding has not yet been developed of the interactions between waves and near-surface fluctuating motions that originate at the free surface. Some of the theoretical and measurement challenges that lie ahead have been highlighted by this present investigation using artificial rain.

4. Conclusions and recommendations

During this laboratory study, the velocity fluctuations in the aqueous layer adjacent to a free surface have been characterized when generated by artificial rain for rain rates between 40 and 170 mm h^{-1}. The attenuation rates of freely propagating gravity water waves exposed to the artificial rain have also been quantified for rain rates of 108 and 141 mm h^{-1}.

The velocity fluctuations generated in the vicinity of the free surface by the rain are isotropic beyond the minimum reliable measurement depth of 30 mm achievable with our instrumentation. The intensities of the measured fluctuating velocities adjacent to the interface are remarkably weak and insensitive to rainfall rate over a range from 40 to 170 mm h^{-1}. Quantitative agreement is found with the independent measurements of Braun (2003).

Measurements obtained by profiling at constant depth yielded wavenumber spectra consistent with conventional turbulence spectrum characterizations. The measured spectra yielded a characteristic aqueous roughness length of 23 mm which was independent of the rainfall rate. However, the measured fluctuations were so weak that the inertial subrange became too narrow for the reliable determination of turbulent dissipation rates.

In the present measurements of monochromatic wave attenuation rates due to viscosity in a wave tank with a clean surface in the absence of rainfall, quantitative agreement is found with theoretical predictions at low wave steepness levels. However, systematic and significant increases in the normalized attenuation rates were observed between mean steepnesses of $AK = 0.10$ and 0.15. These observations are consistent with the high viscous attenuation rates observed by Banner & Peirson (2007) and Tian *et al.* (2010) for grouped waves.

The measurements of wave attenuation rate over a substantial rainfall fetch during the present study support the findings of Tsimplis (1992) that the wave attenuation rate is independent of rainfall rate and wave steepness. The lack of dependence of wave attenuation rates on the rainfall rate is consistent with the observations of weak dependence of the subsurface fluctuating velocity structure and the rain–wave spectrum on rainfall rate.

Based on the literature relating to the interaction of individual droplets with undisturbed liquid interfaces, it is concluded that a near-saturated condition develops at high rainfall rates. Below a threshold rainfall rate, predicted to be in the vicinity of 30 mm h^{-1}, rain-rate-sensitive regimes may exist but very few studies have captured reliable data at such rain rates.

Specific objectives of future studies should include: investigation of droplet-wave-turbulence behaviour at low rainfall rates ($<$30 mm h^{-1}); development of non-intrusive methods for measuring rain-generated capillary waves; and, application of reliable techniques that capture fluctuating velocities at the interface where energy budget considerations show that very strong dissipation occurs.

The measured wave attenuation rates due to rain obtained during this study have been compared quantitatively with other laboratory measurements of wave attenuation processes. At frequencies higher than 4 rad s^{-1}, attenuation due to opposing wind is comparable with active breaking with sufficient wind forcing. Attenuation due to rainfall with intensities lower than 141 mm h^{-1} is relatively weak in comparison with opposing wind and breaking but remains significantly stronger than viscous attenuation at wave frequencies less than 40 rad s^{-1}. Available data are also compared with the theoretical predictions of wave attenuation rates due to subsurface turbulence developed by TB (2002) and AJ (2006). Present theoretical approaches neglect the violent fluctuations of the interface itself, which are shown to be an important consideration when characterizing energy transfer across rain-irradiated water surfaces.

Acknowledgements

The authors would like to express their appreciation for the technical support provided by the staff of the Water Research Laboratory, especially Mrs W. Thomason-Harper, Mrs A. Blacka, Mr H. Studholme and the late Mr J. Hart. Conicyt–Chile and Universidad Politécnica de Valencia-Spain provided scholarship funding for J.F.B. and J.S.P. respectively. Tarbiat Modares University provided partial funding support towards of sabbatical leave for S.A.A. M.L.B. and W.L.P. gratefully acknowledge the support from the Australian Research Council under Discovery Projects 0452505 and 0985602 and the UNSW Faculty of Engineering for providing an equipment grant for the construction of the rain generator. The authors wish to thank the sub-editor and three anonymous reviewers for directing the authors to a number of useful references which significantly improved the rigour and quality of this contribution.

REFERENCES

ARDHUIN, F. & JENKINS, A. D. 2006 On the interaction of surface waves and upper ocean turbulence. *J. Phys. Oceanogr.* **36**, 551–557.

ARDHUIN, F., ROGERS, E., BABANIN, A., FILIPOT, J.-F., MAGNE, R., ROLAND, A., VAN DER WESTHUYSEN, A., QUEFFEULOU, P., LEFEVRE, J.-M., AOUF, L. & COLLARD, F. 2010 Semi-empirical dissipation source functions for wind–wave models: part I, definition, calibration and validation. *J. Phys. Oceanogr.* **40** (9), 1917–1941.

BANNER, M. L. 1988 On the mechanics of spilling zones of quasi-steady breaking water waves. In *Sea Surface Sound* (ed. B. R. Kerman). pp. 63–70. Kluwer.

BANNER, M. L. & PEIRSON, W. L. 2007 Wave breaking onset and strength for two-dimensional deep-water wave groups. *J. Fluid Mech.* **585**, 93–115.

BANNER, M. L. & SONG, J. B. 2002 On determining the onset and strength of breaking for deep water waves. Part II: influence of wind forcing and surface shear. *J. Phys. Oceanogr.* **32**, 2559–2570.

BELCHER, S. E., HARRIS, J. A. & STREET, R. L. 1994 Linear dynamics of wind waves in coupled turbulent air flow. Part 1. Theory. *J. Fluid Mech.* **271**, 119–151.

BELCHER, S. E. & HUNT, J. C. R. 1998 Turbulent flow over hills and waves. *Annu. Rev. Fluid Mech.* **30**, 507–538.

BENJAMIN, T. B. & FEIR, J. E. 1967 The disintegration of wavetrains in deep water, Part 1. *J. Fluid Mech.* **27**, 417–430.

BLIVEN, L., SOBIESKI, P. & CRAEYE, C. 1997 Rain generated ring-waves: measurements and modelling for remote sensing. *Intl J. Remote Sensing.* **18** (1), 221–228.

BOYEV, A. G. 1971 The damping of surface waves by intense turbulence. *Izv. Atmos. Ocean Phys.* **7**, 31–36.

BRADSHAW, P. 1971 *An Introduction to Turbulence and its Measurement*, 1st edn. Pergamon.

BRAUN, N. 2003 Untersuchungen zur Radar-Rückstreuung und Wellendämpfung beregneter Wasseroberflächen, Dissertation, Universität Hamburg, Fachbereich Geowissenschaften. 'On the Radar Backscattering and Wave Damping on Water Surfaces Agitated by Rain'. Dissertation thesis, Hamburg University, Geoscience department.

BURATTINI, P., LAVOIE, P. & ANTONIA, R. A. 2005 On the normalized turbulent energy dissipation rate. *Phys. Fluids* **17**, 098103.

CHEUNG, T. K. & STREET, R. L. 1988 The turbulent layer in the water at an air–water interface. *J. Fluid Mech.* **194**, 133–151.

COLLARD, F., ARDHUIN, F. & CHAPRON, B. 2009 Monitoring and analysis of ocean swell fields using a spaceborne SAR: a new method for routine observations. *J. Geophys. Res.* **114**, C07023.

CRAEYE, C. & SCHLÜSSEL, P. 1998 Rainfall on the sea: surface renewals and wave damping. *Boundary-Layer Meteorol.* **89**, 349–355.

CRAIG, P. & BANNER, M. 1994 Modelling wave-enhanced turbulence in the ocean surface layer. *J. Phys. Oceanogr.* **24**, 2546–2559.

CSANADY, G. T. 1990 The role of breaking wavelets in air–sea gas transfer. *J. Geophys. Res.* **95**, 749–759.

DORE, B. D. D. 1978 Some effects of the air–water interface on gravity waves. *Geophys. Astrophys. Fluid Dyn.* **10** (1), 215–230.

DRAZEN, D. A., MELVILLE, W. K. & LENAIN, L. 2008 Inertial scaling of dissipation in unsteady breaking waves. *J. Fluid Mech.* **611**, 307–332.

DUNCAN, J. H. 1981 An experimental investigation of breaking waves produced by a towed hydrofoil. *Proc. R. Soc. Lond.* A **377**, 331–348.

DUNCAN, J. H. 1983 The breaking and non-breaking wave resistance of a two-dimensional hydrofoil. *J. Fluid Mech.* **126**, 507–520.

FEDORCHENKO, A. I. & WANG, A.-B. 2004 On some common features of drop impact on liquid surfaces. *Phys. Fluids* **16** (5), 1349–1365.

GEMMRICH, J. 2010 Strong turbulence in the wave crest region. *J. Phys. Oceanogr.* **40** (3), 583–595.

GORDILLO, J. M. & GEKLE, S. 2010 Generation and breakup of Worthington jets after cavity collapse. Part 2. Tip breakup of stretched jets. *J. Fluid Mech.* **663**, 331–346.

GREEN, T. & HOUK, D. F. 1979 The mixing of rain with near-surface water. *J. Fluid Mech.* **90** (3), 569–588.

HARRIS, J. A., BELCHER, S. E. & STREET, R. L. 1996 Linear dynamics of wind waves in coupled turbulent air–water flow. Part 2. *J. Fluid Mech.* **308**, 219–254.

HO, D. T., ASHER, W. E., BLIVEN, L. F., SCHLOSSER, P. & GORDAN, E. L. 2000 On the mechanisms of rain-induced air–water gas exchange. *J. Geophys. Res.* **105** (C10), 24045–24057.

HOUK, D. F. & GREEN, T. 1976 A note on surface waves due to rain. *J. Geophys. Res.* **81**, 4482–4484.

HUNT, J. & GRAHAM, J. 1978 Free-stream turbulence near plane boundaries. *J. Fluid Mech.* **84**, 209–235.

JENKINS, A. D. 1987 Wind and wave induced currents in a rotating sea with depth-varying eddy viscosity. *J. Phys. Oceanogr.* **17**, 938–951.

JIANG, J.-Y., STREET, R. L. & KLOTZ, S. P. 1990 A study of wave–turbulence interaction by use of a nonlinear water wave decomposition technique. *J. Geophys. Res.* **95**, 16037–16054.

JONES, I. S. F. & TOBA, Y. 2001 *Wind Stress Over the Ocean*. Cambridge University Press.

KOMORI, S., NAGAOSA, R. & MURAKAMI, Y. 1993 Turbulence structure and mass transfer across a sheared air–water interface in wind-driven turbulence. *J. Fluid Mech.* **249**, 161–183.

LAMB, H. 1932 *Hydrodynamics*. Cambridge University Press, 738 pp.

LANGE, P. A., VAN DER GRAAF, G. & GADE, M. 2000 Rain-induced subsurface turbulence measured using image processing methods. In *Proc. Intl Geosci. Remote Sens. Symp. (IGARSS)'00*, pp. 3175–3177. IEEE.

LE MÉHAUTÉ, B. 1988 Gravity–capillary rings generated by water drops. *J. Fluid Mech.* **197**, 415–427.

LE MÉHAUTÉ, B. & KHANGAONKAR, T. 1990 Dynamic interaction of intense rain with water waves. *J. Phys. Oceanogr.* **20**, 1805–1812.

LENEWEIT, G., KOEHLER, R., ROESNER, K. G. & SCHÄFER, G. 2005 Regimes of drop morphology in oblique impact on deep fluids. *J. Fluid Mech.* **543**, 303–331.

LIOW, J. L. 2001 Splash formation by spherical drops. *J. Fluid Mech.* **427**, 73–105.

LONGUET-HIGGINS, M. S. 1994 Shear instability in spilling breakers. *Proc. R. Soc. Lond.* A **446**, 399–409.

MAGNAUDET, J. & THAIS, L. 1995 Orbital rotational motion and turbulence below laboratory wind water waves. *J. Geophys. Res.* **100** (C1), 757–771.

MANTON, M. J. 1973 On the attenuation of sea waves by rain. *J. Geophys. Fluid Dyn.* **5**, 249–260.

MARSHALL, J. S. & PALMER, W. MCK. 1948 The distribution of raindrops with size. *J. Meteorol.* **5**, 165–166.

MITSUYASU, H. & HONDA, T. 1982 Wind-induced growth of water waves. *J. Fluid Mech.* **123**, 425–442.

NIKORA, V. & GORING, D. 1998 ADV measurements of turbulence: can we improve their interpretation? *J. Hydraul. Engng ASCE* **124–6**, 630–634.

NYSTUEN, J. 1990 A note on the attenuation of surface gravity waves by rainfall. *J. Geophys. Res.* **95**, 18353–18355.

OKAWA, T., SHIRAISHI, T. & MORI, T. 2008 Effect of impingement angle on the outcome of single water drop impact onto a plane water surface. *Exp. Fluids* **44**, 331–339.

ÖLMEZ, H. & MILGRAM, J. 1992 An experimental study of attenuation of short water waves by turbulence. *J. Fluid Mech.* **238**, 133–156.

PEIRSON, W. L. & BANNER, M. L. 2000 On the strength of breaking of deep water waves. In *Coastal Engineering 2000* (ed. R. Cox). pp. 369–381. ASCE.

PEIRSON, W. L. & GARCIA, A. W. 2008 On the wind-induced growth of slow water waves of finite steepness. *J. Fluid Mech.* **608**, 243–274.

PEIRSON, W. L., GARCIA, A. W. & PELLS, S. E. 2003 Water–wave attenuation due to opposing wind. *J. Fluid Mech.* **487**, 345–365.

POON, Y., TANG, S. & WU, J. 1992 Interactions between rain and wind waves. *J. Phys. Oceanogr.* **22**, 976–987.

POPE, S. 2000 *Turbulent Flows*. Cambridge University Press.

PROSPERETTI, A. & OGUZ, H. N. 1993 The impact of drops on liquid surfaces and the underwater noise of rain. *Annu. Rev. Fluid Mech.* **25**, 577–602.

RAPP, R. J. & MELVILLE, W. K. 1990 Laboratory measurements of deep water breaking waves. *Phil. Trans. R. Soc. Lond.* A **331**, 735–800.

REYNOLDS, O. 1874 On the action of rain to calm the sea. *Proc. Lit. Phil. Soc. Manchester*, Vol. 14, Session 1874–5.

SHELTON, C. H., VON BERNUTH, R. D. & RAJBHANDARI, S. P. 1985 A continuous application rainfall simulator. *A S AE.* **28** (4), 1115–1119.

SIDDIQUI, K. & LOEWEN, M. R. 2007 Characteristics of the wind drift layer and microscale breaking waves. *J. Fluid Mech.* **573**, 417–456.

TEIXEIRA, M. A. C. & BELCHER, S. E. 2002 On the distortion of turbulence by a progressive surface wave. *J. Fluid Mech.* **458**, 229–267.

TENNEKES, H. & LUMLEY, J. L. 1972 *A First Course in Turbulence*. MIT.

TIAN, Z., PERLIN, M. & CHOI, W. 2010 Energy dissipation in two-dimensional unsteady plunging breakers and an eddy viscosity model. *J. Fluid Mech.* **655**, 217–257.

TOLMAN, H. 2009 User manual and system documentation of WAVEWATCH III TM version 3.14. *Tech. Note. MMAB Contribution* 276. NOAA.

TSIMPLIS, M. N. 1992 The effect of rain in calming the sea. *J. Phys. Oceanogr.* **22**, 404–412.

TSIMPLIS, M. & THORPE, S. A. 1989 Wave damping by rain. *Nature* **342**, 893–895.

VAN DORN, W. G. 1966 Boundary dissipation of oscillatory waves. *J. Fluid Mech.* **24**, 769–779.

VOULGARIS, G. & TROWBRIDGE, J. 1998 Evaluation of the acoustic Doppler velocimeter (ADV) for turbulence measurements. *J. Atmos. Ocean Technol.* **15**, 272–289.

WILSON, W. S., BANNER, M. L., FLOWER, R. J., MICHAEL, J. A. & WILSON, D. G. 1973 Wind-induced growth of mechanically generated water waves. *J. Fluid Mech.* **58**, 435–460.

YARIN, A. L. 2006 Drop impact dynamics: splashing, spreading, receding, bouncing. *Annu. Rev. Fluid Mech.* **38**, 159–192.

ZAPPA, C. J., HO, D. T., MCGILLIS, W. R., BANNER, M. L., DACEY, J. W. H., BLIVEN, L. F., MA, B. & NYSTUEN, J. 2009 Rain-induced turbulence and air–sea gas transfer. *J. Geophys. Res.* **114**, C07009.